Ocean Engineering 358 (2026) 125861

Contents lists available at ScienceDirect

Ocean Engineering

journal homepage: www.elsevier.com/locate/oceaneng

Research paper

Investigating the mechanisms of motion response amplification for a cylindrical FPSO under wave-current coupling

Min Li [a], Da Li [b], Shenglei Fu [b], Yuan Zhuang [a,*], Decheng Wan [a]

[a] Computational Marine Hydrodynamics Lab, School of Ocean and Civil Engineering, Shanghai Jiao Tong University, Shanghai, 200240, China
[b] CNOOC Research Institute, Beijing, China

ARTICLE INFO

Keywords:
Cylindrical FPSO
Wave-current coupling
Motion amplification
Vortex evolution

ABSTRACT

Cylindrical Floating Production Storage and Offloading (CFPSO) units show broad prospects in deep-sea oil and gas development due to their cost-effectiveness and adaptability, with their operational safety heavily reliant on motion and load performance. Existing research has primarily focused on wave-only conditions and fully coupled environments, while systematic analysis of the load amplification mechanisms under typical wave–current coupling remains lacking. To address this, this study simulates the motion responses of a CFPSO under wave-only and wave–current coupling conditions. The results show that the current's steady resistance shifts the structure's equilibrium position and selectively amplifies the motion and load dynamics. The ratio of current velocity to wave celerity (Uc/C) is a key parameter for quantifying this amplification effect. The amplification mechanisms differ for various motion directions due to changes in the flow field. The dynamic amplification of heave is directly related to intense random pressure fluctuations induced by complex vortex shedding near the bottom. This study provides a theoretical basis for the structural design and safety assessment of CFPSOs under complex sea conditions.

1. Introduction

Floating Production Storage and Offloading (FPSO) units are critical infrastructure for deep-sea oil and gas development, as their operational stability significantly impacts the safety and efficiency of oil field operations (Zhuang et al., 2022). Among various FPSO configurations, the cylindrical FPSO (CFPSO) is a novel floating platform type (Afriana, 2011; Amin et al., 2022). It offers advantages such as simple structural design, high internal space utilization, and the ability to orient environmental loads without complex turret mooring systems, thereby reducing construction costs and demonstrating strong engineering potential. However, CFPSOs face hydrodynamic challenges, particularly because their inherent heave period often aligns with common wave periods, leading to pronounced heave motion responses that affect platform performance (Hong et al., 2011; Ji et al., 2019).

Throughout the lifecycle of an FPSO, waves and currents are the primary environmental loads. In real sea conditions, they often interact, forming complex wave-current coupling fields (Dutta and Afzal, 2024). This coupling effect is not a simple superposition of wave and current forces but involves nonlinear interactions that alter wave propagation characteristics and flow field structures. For example, it can cause changes in wave height and wavelength, enhance flow separation, and significantly influence the overall loads on the platform. Experimental studies by Li et al. (2024) revealed that wave-current coupling induces low-frequency phase shifts and energy redistribution, increasing surge motion by approximately 30%. Deng et al. (2022a,b) observed that wave-current coupling amplifies heave and roll motions markedly, with quasi-lock-in phenomena caused by vortex shedding from the bottom. These nonlinear effects can exceed the predictions of traditional design methods, posing serious threats to platform safety and structural integrity. Therefore, investigating the amplification mechanisms of wave-current coupling on CFPSO motions and loads is crucial for improving the design reliability and operational safety of such platforms.

In marine engineering, significant understanding has been achieved regarding the dynamic responses of other structures under wave-only and wave-current coupled conditions. For instance, P Wang et al. (2024); W Wang et al. (2024); compared the slamming characteristics of hourglass-shaped and cylindrical floaters using CFD simulations. They found that variations in wave period intensify slamming severity, with a

* Corresponding author.
E-mail address: nana2_0@sjtu.edu.cn (Y. Zhuang).

https://doi.org/10.1016/j.oceaneng.2026.125861
Received 15 March 2026; Received in revised form 14 April 2026; Accepted 30 April 2026
Available online 3 May 2026

pressure peak increase of approximately 25%, highlighting the modulating effect of wave parameters on nonlinear responses. Similarly, Kong et al. (2025) applied the IDDES method to a floating turbine, demonstrating that increasing the wave period from 0.8 s to 1.2 s amplifies power coefficient fluctuations by about 25%, underscoring parametric sensitivity. Under wave-current coupling, the response of other structures becomes more complex. Ni et al. (2025) derived steady-state solutions for wave-current interactions via CFD, revealing significant influences of wave-current angle, wave steepness, and relative water depth on wavelength and wave height. When wave steepness exceeds 0.05, nonlinear effects intensify, leading to wave amplification and errors in linear theory predictions. Zhou et al. (2022) systematically analyzed the heave response of a horizontal floating cylinder under varying wave periods and current velocities. They observed that increasing wave periods reduce vibration amplitudes, while current variations can induce resonance, significantly amplifying motion responses. Li et al. (2023) investigated a Floating Offshore Wind Turbine (FOWT) platform, noting that enlarging the wave-current angle from 0° to 90° increases transverse motion and enhances Vortex-Induced Motion (VIM). Interactions between wave parameters and current velocities may raise the interaction factor above 1.35. Similarly, W Li et al. (2025); S Li et al., 2025 numerically simulated an FOWT under wave-current coupling, finding that waves suppress VIM by shifting the dominant force frequency to the wave frequency, while currents amplify wave dynamics and increase wave loads.

Focusing on FPSOs, research on their dynamic characteristics under wave-only conditions has revealed specific risks. Yang et al. (2025) developed a semi-analytical model for an FPSO with a damping plate, showing that geometric parameters and dissipation coefficients significantly affect heave motion and wave loads. Increasing the damping plate radius amplifies wave loads but suppresses resonance, while dissipation coefficients mitigate nonlinear abruptness at resonant frequencies, enhancing computational stability. Cui et al. (2025) employed 3D potential flow simulations to study a cylindrical FPSO with ring slots, demonstrating that slot geometry modulates heave and pitch performance. Specific parameter combinations can trigger parametric resonance, amplifying pitch motion by up to 120.98%. Their work emphasizes the importance of time-varying restoring stiffness in capturing nonlinear coupling and identifies resonance risks when wave periods approach the system's natural period. Studies have been conducted to investigate the slamming pressure and dynamic response of cylindrical FPSOs under wave-current coupling conditions. Yu et al. (2025) found that increased current velocity shortens the effective wave period, enhances wave run-up and dynamic pressure, and results in coupled responses significantly exceeding linear superposition. Experimental studies, such as Deng et al. (2022a,b), observed notable motion amplification across all six degrees of freedom under wave-current conditions, particularly in cross-flow motion due to VIM. Li et al. (2024) conducted wave tank tests, revealing that wave-current coupling induces low-frequency phase shifts and energy redistribution, increasing surge motion by approximately 30%. Additionally, Huo et al. (2023) validated via CFD that wave-current coupling can suppress or enhance VIM, with vortex visualization elucidating energy dissipation mechanisms.

Despite these advancements, current research has significant limitations. Most studies, parameter analyses often fix wave spectra or current speeds, failing to systematically vary wave periods and currents as independent variables to quantify their interactions, and lack comprehensive parameter space scanning. Mechanistic understanding is insufficient, as nonlinear dynamics and parameter coupling effects are not deeply explored. Therefore, for CFPSOs, there is an urgent need to use parametric CFD simulations and experiments to systematically study the quantitative impact of different wave periods and current speeds on wave-current coupling amplification effects. Moreover, revealing the underlying mechanisms, particularly from the perspective of flow field evolution to explain the physical roots of motion and load amplification remains underdeveloped.

This study employs CFD methods to investigate the amplification effects of wave-current coupling on the motion and loads of an FPSO. Based on the open-source framework OpenFOAM, it integrates a buoyancy-modified k-omega SST turbulence model and a self-developed six-degree-of-freedom motion module to numerically simulate the structure's motions and loads. The research analyzes and presents the motion and load responses of the FPSO, quantifies amplification effects, and elucidates the generating mechanisms through detailed flow field analysis. This work provides theoretical support and data references for the hydrodynamic characteristics of FPSOs under complex coupled sea conditions, offering key insights for structural design.

2. Numerical methods

A high-fidelity numerical model was developed to simulate the hydrodynamic response of a cylindrical FPSO under complex wave-current interactions. The simulations were performed using an incompressible two-phase flow CFD solver, naoe-FOAM-SJTU (Zhao et al., 2020; Wang and Wan, 2018; Wang et al., 2019), which is built upon the open-source CFD platform OpenFOAM. The six-degree-of-freedom (6-DOF) motion responses are calculated using an in-house developed rigid body motion solver. The mooring system dynamics are simulated using a spring model (Liu and Wan, 2013). The free surface is captured by the Volume of Fluid (VOF) method (Hirt and Nichols, 1981), while turbulence effects are modeled using the buoyancy-modified k-ω SST (Menter, 1994) turbulence model. For effective wave boundary conditions, the relaxation zone technique is implemented through the wave2foam toolbox to ensure numerical stability in wave generation and absorption (Higuera et al., 2013). A uniform current condition is superimposed throughout the flow field to reproduce combined wave-current scenarios.

2.1. Governing equations and turbulence model

This study employs the standard k-omega SST turbulence model proposed by Menter (2003) to close the Reynolds-Averaged Navier--Stokes (RANS) equations. The model demonstrates good predictive accuracy for near-wall flows and free shear flows, making it widely used in engineering calculations and scientific simulations. However, when applied to two-phase flow simulations involving wave-current interactions, the standard k-omega SST model faces a significant issue: at the gas-liquid interface, the sharp density variation leads to a sharp increase in the velocity gradient, which in turn causes an unphysical rise in turbulent kinetic energy and turbulent viscosity. This abnormal increase results in excessive numerical dissipation, manifested as unrealistic damping of wave amplitude, where the attenuation exceeds actual physical conditions, seriously compromising simulation accuracy.

To address this drawback, following the approach of Van Maele and Merci (2006), a buoyancy correction term based on the Standard Gradient Diffusion Hypothesis (SGDH) is introduced into the turbulent kinetic energy (TKE) transport equation to properly account for the effect of abrupt density changes at the two-phase interface on turbulence characteristics. This modification effectively suppresses the unphysical growth of turbulence quantities near the interface, thereby improving the simulation results under wave-current coupling conditions. Based on the above considerations, the turbulent kinetic energy equation used after incorporating the buoyancy modification into the standard k-omega SST model is presented as follows:

$$\frac{\partial \rho k}{\partial t}+\frac{\partial \rho u_j k}{\partial x_j}-\frac{\partial}{\partial x_j}\left[\rho(\nu+\sigma_k \nu_l)\frac{\partial k}{\partial x_j}\right]=\rho P_k+G_b-\rho\beta^* \omega k \tag{1}$$

$$\frac{\partial \omega}{\partial t}+\frac{\partial u_j \omega}{\partial x_j}-\frac{\partial}{\partial x_j}\left[(\nu+\sigma_\omega \nu_t)\frac{\partial \omega}{\partial x_j}\right]=\frac{\gamma}{\nu_t}G-\beta\omega^2+2(1-F_1)\frac{\sigma_{\omega 2}}{\omega}\frac{\partial k}{\partial x_j}\frac{\partial \omega}{\partial x_j} \tag{2}$$

$$G_b = -\frac{\nu_t}{\sigma_t}\frac{\partial\rho}{\partial x_j}g_j \tag{3}$$

$$\nu_t = \frac{a_1 k}{\max(a_1\omega, SF_2)}, \tag{4}$$

where, Equation (1) is referred to as the buoyancy-corrected Turbulent Kinetic Energy Transport Equation; Equation (2) is the transport equation for the turbulent dissipation rate Omega. ν the fluid kinematic viscosity, ν_t is the turbulent kinematic viscosity, F_1 is the first blending function. β^*, β, σ_k, σ_ω, $\sigma_{\omega 2}$, γ are constants in the turbulence model. S is the mean strain rate of the flow velocity; F_2 is the second blending function; a_1 is a model constant. σ_t is a scalar constant that determines the degree of buoyancy correction; when dealing with two-phase flow of water and air, its value is typically taken as 0.85.

2.2. Numerical wave-current generation and absorption

The wave2foam toolbox (Jacobsen et al., 2012) utilizes a relaxation zone-based numerical method for the generation of waves and currents. This approach establishes relaxation zones within specific regions of the fluid computational domain. Through a relaxation function, the flow field variables, namely velocity and free-surface elevation, are gradually adjusted towards target values of the wave-current field determined by theoretical wave models. This process facilitates the gradual formation and propagation of the desired waves and currents within the computational domain. Compared to methods such as piston-type or flap-type wavemakers, which require mesh movement or internal momentum sources, the relaxation zone method offers simpler implementation, eliminates the need for mesh deformation, allows for convenient simulation of complex environments involving combined waves and currents, and provides good numerical stability.

In numerical wave tanks, the computational domain is finite. If the outlet boundary is left untreated, waves propagating to the boundary will reflect. These reflected waves re-enter the computational domain and interfere with the flow field results, making wave absorption at the outlet essential. The wave2foam toolbox also employs relaxation zones for wave absorption. Specifically, an absorption relaxation zone is defined near the domain outlet, and an artificial damping source term is added to the momentum equations within this zone. This damping term suppresses the wave motion, causing the wave energy entering the zone to be gradually dissipated. As a result, the wave height and velocity decay smoothly to zero, effectively mitigating wave reflection. The coordinated use of relaxation zones at the inlet and outlet collectively ensures the accuracy and stability of wave-current simulations within the numerical wave tank (Higuera et al., 2012).

Under combined wave-current conditions, the water particle velocities at the inlet boundary of the computational domain can be obtained by the linear superposition of the analytical solution from wave potential theory and the steady current velocity. This study focuses on first-order Stokes regular waves, assuming unidirectional wave propagation. With reference to the still water level, the surface elevation equation and water particle velocity expressions for regular waves are given as follows:

$$\eta = \frac{H}{2}\cos(kx - \omega t + \varphi) \tag{5}$$

In this study, the current direction is consistent with the wave propagation direction. Therefore, the horizontal velocity component is obtained by superimposing the wave-induced velocity and the steady current velocity:

$$\text{Horizontal velocity}: u = \frac{\pi H}{T}\frac{\cosh k(z+d)}{\sinh kd}\cos(kx - \omega t + \varphi) + u_{current} \tag{6}$$

$$\text{Vertical velocity}: w = \frac{\pi H}{T}\frac{\sinh k(z+d)}{\sinh kd}\sin(kx - \omega t + \varphi) \tag{7}$$

where, H is the wave height. T is the wave period. k is the wave number. d is the water depth. ω is the wave angular frequency ($\omega = 2\pi/T$). t is the current time. η is the surface elevation at the corresponding time. $u_{current}$ the current velocity.

3. Numerical step

3.1. Geometry and computational domain

The geometric model used in this study is a cylindrical FPSO unit based on a 1:60 scale ratio. The geometry of the numerical model is shown in Fig. 1. The principal dimensions and mass properties of the model are summarized in Table 1. The cylindrical hull has a diameter of 1.45 m and a draft of 0.367 m at model scale, resulting in a depth-to-draft ratio of approximately 2.04. The corresponding full-scale displacement is about 145.5 kt. The main body of the model is cylindrical, and its bottom edge is designed with serrated heave plates to enhance motion stability. Fig. 1(b) provides a bottom view of the model, clearly illustrating the bottom structure, which includes a smooth central region and three surrounding heave plates with serrated edges. Two of these heave plates are shown in a trimmed configuration.

A horizontal stiff mooring system was employed to restrain the cylindrical FPSO in this study. The mooring system consists of four evenly distributed mooring lines, arranged to satisfy symmetry requirements. Table 2 details the fairlead and anchor point coordinates, unstretched length, extended length under pretension, and axial stiffness for each mooring line. The configuration of the mooring system is illustrated in Fig. 2. To maintain consistency with experimental data and focus on the main motion response under wave-current interactions, the dynamic drag force and gravity effects of the mooring lines are neglected. This simplified approach is widely applicable for motion performance analysis of deep-water floating structures.

This study employs a simplified linear spring model for the mooring system, which omits the dynamic damping and nonlinear catenary restoring effects of the mooring lines. We acknowledge that this simplification has known limitations. As shown in the comparative study by Kim et al. (2013), the linear spring method cannot fully capture the additional damping from mooring lines or complex coupled stiffness effects, such as surge-pitch coupling. These limitations are particularly relevant when predicting very low-frequency dynamics or precise mean offsets, especially if the mooring system represents a significant portion of the total mass. However, the same study by Kim et al. (2013) also indicates that when the mooring system's influence on wave-frequency dynamics is relatively small, the difference in motion predictions between the linear spring method and a high-fidelity nonlinear finite element method is minimal. This finding supports the use of the simplified model for analyzing dominant wave-frequency responses.

The primary objective of this work is to clarify the fundamental wave-current interaction mechanisms that control wave-frequency motion and load amplification of the bare hull. For this purpose, using a simplified mooring system is a well-established approach. It allows us to directly attribute the observed amplification effects to changes in the flow field and vortex dynamics around the hull, rather than to complex mooring line behavior. Therefore, given our focus on wave-frequency mechanisms driven by hull-flow interaction, the chosen simplified mooring model is appropriate and sufficient for this investigation.

This study employs a numerical wave tank with dimensions of 30 m in length, 16 m in width, and 7.25 m in height. The water depth is set at 5.25 m, satisfying deep-water wave conditions, with the specific configuration shown in Fig. 2. For wave simulation, the relaxation zone method is adopted for wave generation and absorption. The wave generation zone is 6 m long, and the wave absorption zone is 13 m long. The

Fig. 1. Geometric model of the FPSO (a) Side view; (b) Bottom view; (c) Perspective view.

Table 1
The principal dimensions and mass properties of the model.

Parameter	Symbol	Model Scale	Full Scale
Diameter	D	1.45m	87.0m
Draft	T	0.367 m	22.0 m
Depth	H	0.75 m	45.0 m
Displacement	Δ	674.7 kg	145,466.8 t
Vertical Center of Gravity (from base)	KG	0.354 m	21.25 m
Radius of gyration (Roll/pitch)	k_{yy}	0.497 m	29.8 m
Radius of gyration (yaw)	k_{zz}	0.605 m	36.3 m
Heave Plate Thickness	T_p	0.042m	2.5 m

computational domain employs a velocity inlet boundary condition at the inlet, where both wave and current conditions are prescribed. The outlet is set as a pressure outlet with zero static pressure to allow free outflow. The top boundary is defined as an atmospheric pressure boundary. The two side boundaries are defined as symmetry planes to simulate an infinitely wide domain. The computational domain for wave-current coupled conditions remains consistent with that of the pure wave scenario.

Regarding mesh generation, Fig. 3 displays the grid distribution on the XOY and YOZ planes, as well as the surface mesh on the FPSO. To accurately capture the boundary layer effects under wave-current interactions, a boundary layer grid technology was implemented. The height of the first grid layer was set at 0.001 m. This configuration ensured that the dimensionless wall distance (y+) remained within the optimal range of 30-100 throughout the simulation. The total grid count reached approximately 5.3 million for the wave-only condition and 5.39 million for the combined wave-current condition, meeting the accuracy requirements for different working conditions.

3.2. Grid independence study

To ensure the reliability and accuracy of the simulation, a grid independence study was carried out using three sets of grids with coarse, medium, and fine densities. The coarse grid size was set to 1.2 times that of the medium grid, while the fine grid size was 0.8 times that of the medium grid. The corresponding grid numbers were 2.97 million, 5.39 million, and 9.11 million, respectively. Fig. 4 presents a comparison of the time history curves of surge, heave, and pitch motion responses under the three grid sizes. The results show that motion responses under all grid densities exhibit consistent periodic variation patterns, with only minor differences in amplitude. This indicates that the numerical results are insensitive to grid density, confirming grid independence.

Table 3 lists the mean values of surge, heave, and pitch motion responses for different grid numbers. The difference in the mean surge response between the fine and medium grids is only 1.1%, and the difference in the mean pitch response is 0.2%. These small deviations indicate that further grid refinement has limited influence on the results, demonstrating good convergence. The mean heave offset is very small, about 0.1% of the model diameter. The differences seen between grids are within the expected numerical error for such a small value, and the results show a clear converging trend. This indicates the grid resolution is sufficient to determine this static position. The main purpose of the grid study is to verify the reliability of the dynamic motion responses, which are the focus of this paper. The convergence of these motion amplitudes has been confirmed. Since the forces that cause the motions are integrals of pressure on the hull, the convergence of the motions strongly suggests that the key features of the underlying pressure field, especially those driving the motion, are also resolved well by the chosen

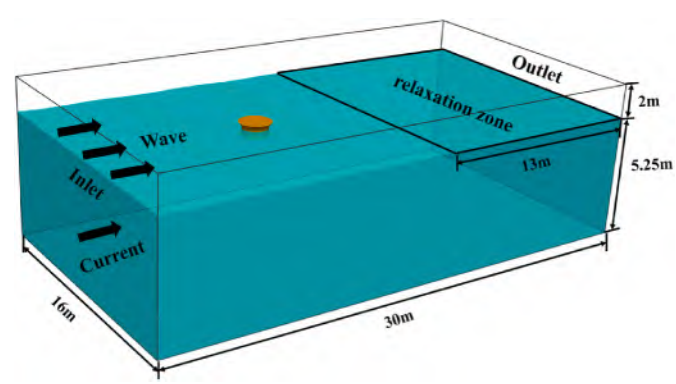

Fig. 2. Computational domain.

Table 2
The mooring configuration.

Line number	Location	X (m)	Y (m)	Z (m)	Length under Pretension(m)	Length (m)	Stiffness (kN/m)
Line1	Anchor Point	0.518	−0.518	0	3.24	2.5	0.121
	fairlead	2.816	−2.816	0	3.24	2.5	0.121
Line2	Anchor Point	0.518	0.518	0	3.24	2.5	0.121
	fairlead	2.816	2.816	0	3.24	2.5	0.121
Line3	Anchor Point	−0.518	0.518	0	3.24	2.5	0.121
	fairlead	−2.816	2.816	0	3.24	2.5	0.121
Line4	Anchor Point	−0.518	−0.518	0	3.24	2.5	0.121
	fairlead	−2.816	−2.816	0	3.24	2.5	0.121

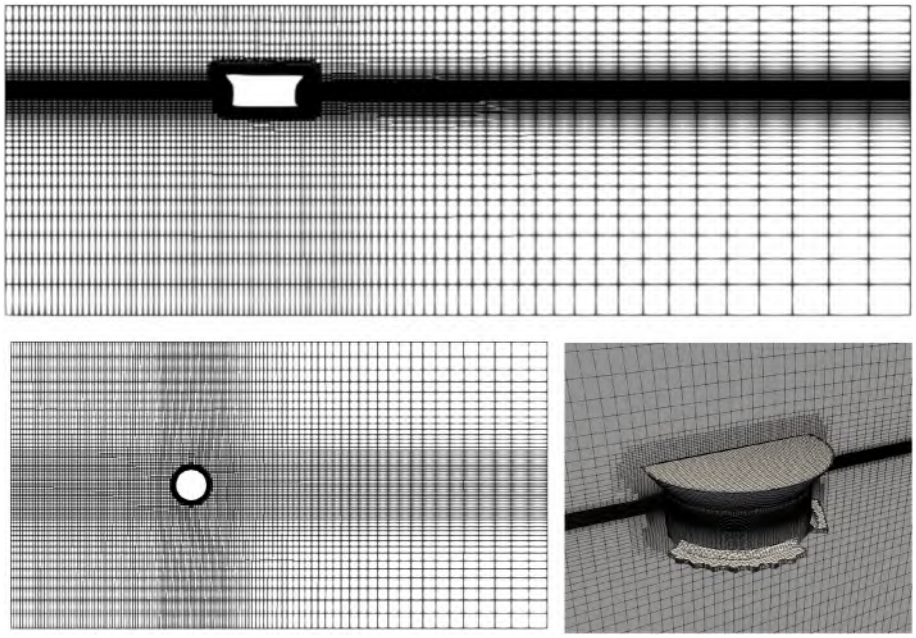

Fig. 3. Computational mesh (a) Overview on x-z plane (y = 0); (b) Overview on x-y plane (z = 0); (c) Magnified view on FPSO.

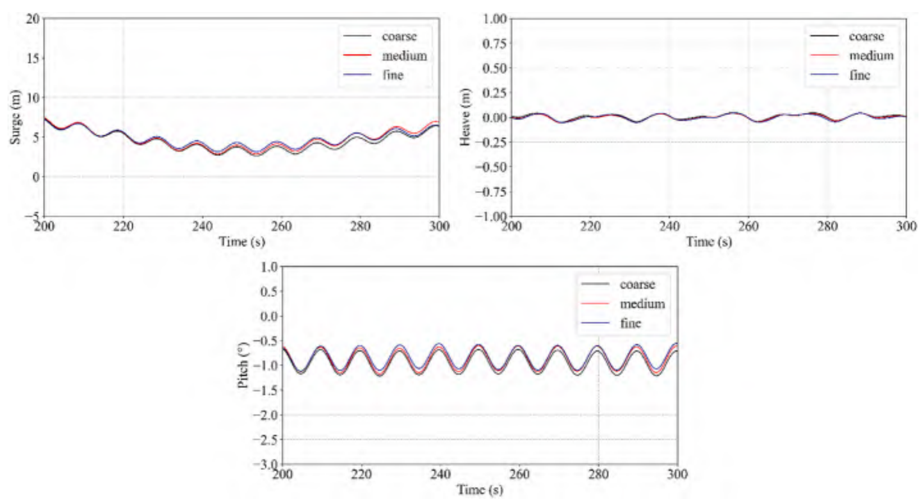

Fig. 4. Comparison between different mesh resolutions (a)Surge; (b) Heave; (c) Pitch.

Table 3
Parameters in mesh convergence study.

Item	Cell number	Surge (m)	Heave (m)	Pitch (°)
Coarse	2,972,637	5.215	0.009	−0.948
Medium	5,390,581	5.366	0.003	−0.919
Fine	9,110,859	5.430	0.002	−0.917

grid. Considering both computational accuracy and efficiency, the medium grid was selected for subsequent numerical simulations. This choice ensures reasonable computational speed while maintaining result accuracy.

3.3. Validation against experimental data

To validate the accuracy of the numerical model, a systematic comparison was carried out between the numerical results and corresponding experimental data under seven wave periods: 7s, 10s, 12s, 14s, 16s, 18s, and 20s. The experimental data used for CFD validation in this study were obtained from a dedicated model test campaign. The tests were conducted in the SJTU Towing Tank. Fig. 5 presents a comparison of the Response Amplitude Operators (RAOs) for surge, heave, and pitch motions obtained from the numerical simulations and model tests.

The results show that the RAO curves from the numerical calculations agree well with the experimental measurements in both trend and magnitude across all wave periods. In particular, the response amplitudes match closely between the numerical and experimental data. The deviations are small under each wave period, indicating that the numerical model can effectively capture the actual motion characteristics.

Based on the consistent agreement observed across the seven wave conditions, it is concluded that the numerical method used in this study provides reliable predictions of the structural motions. This validates the reliability of the numerical model and supports its use in subsequent analyses.

3.4. Simulation matrix

A total of 14 numerical simulation cases, as detailed in Table 4, were

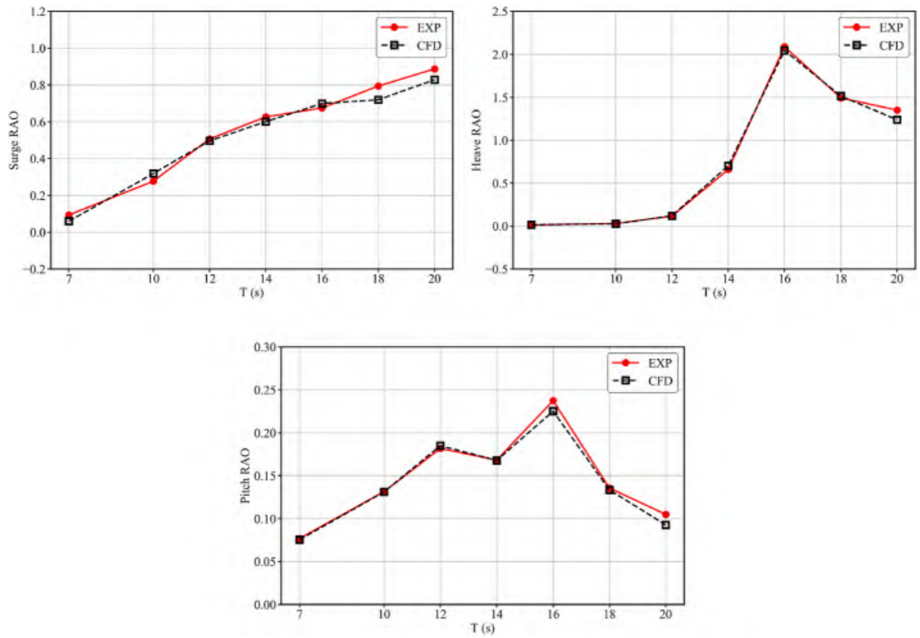

Fig. 5. Comparison between numerical simulation results and experimental results.

designed in this study to systematically investigate the hydrodynamic responses of a cylindrical FPSO under pure wave, and wave-current coupling conditions. The focus was placed on the effect of wave-current coupling on the structural motions. The case setup is described as follows. For each of the five different wave periods, corresponding pure wave cases and wave-current coupled cases were constructed. The wave height was consistently set to 0.05 m at model scale across all wave cases to ensure consistent wave conditions. A current velocity of 0.2 m/s (equivalent to 1.5492 m/s at full scale), which represents the maximum speed encountered under conventional conditions in the South China Sea, was adopted in the wave-current coupling cases to enable a meaningful comparison of structural responses under combined environmental loading. To examine the gradient effect of current velocity, two lower speeds (0.1 m/s and 0.05 m/s) were added for the 14s wave period. These correspond to 50% and 25% of the original 0.2 m/s condition, forming a velocity series that clarifies how amplification initiates and scales with current speed. The selected speeds also represent typical low-to-moderate currents, extending the practical relevance of the study. To further examine the influence of current velocity variation on the coupling effect, additional wave-current cases under low and medium current velocities were added for selected wave periods. These cases help evaluate the impact of current velocity on the coupling behavior. Overall, the case matrix systematically covers both pure wave and wave-current coupling conditions across a range of wave periods and current velocities, forming a comprehensive parametric framework for investigating their coupled effects. This setup allows a multi-perspective analysis of the potential dynamic amplification phenomenon and its underlying mechanisms during wave-current interactions.

4. Results and discussion

4.1. Wave-current coupling effects across different wave periods

The motion responses of an FPSO are of critical importance as they directly impact its structural safety, operational efficiency, and station-keeping system design. In this study, the influence of wave-current coupling is analyzed in terms of its effect on both the mean position and the dynamic oscillatory response of the structure. The alteration of the dynamic response is quantitatively assessed. This assessment is performed by calculating the relative change (expressed as a percentage) in the response amplitude from the pure wave condition to the wave-current condition, under identical wave parameters. Figs. 6, 7 and 8 compares the motion responses of a cylindrical FPSO under pure wave conditions and wave-current coupling conditions across different wave

Table 4
An Typical load conditions in model test.

Case number	Case	Current velocity(m/s)		Wave height (m)		Wave period (s)	
		Model Scale	Full Scale	Model Scale	Full Scale	Model Scale	Full Scale
1	C0W10	/	/	0.05	3	1.2910	10
2	C0W12	/	/	0.05	3	1.5492	12
3	C0W14	/	/	0.05	3	1.8074	14
4	C0W16	/	/	0.05	3	2.0656	16
5	C0W18	/	/	0.05	3	2.3238	18
6	C0W20	/	/	0.05	3	2.5820	20
7	C2W10	0.2	1.5492	0.05	3	1.2910	10
8	C2W12	0.2	1.5492	0.05	3	1.5492	12
9	C2W14	0.2	1.5492	0.05	3	1.8074	14
10	C2W16	0.2	1.5492	0.05	3	2.0656	16
11	C2W18	0.2	1.5492	0.05	3	2.3238	18
12	C2W20	0.2	1.5492	0.05	3	2.5820	20
13	C1W14	0.1	0.7746	0.05	3	1.8074	14
14	C05W14	0.05	0.3873	0.05	3	1.8074	14

periods, focusing on surge, heave, and pitch motions, including both the mean values and amplitudes. Within the investigated parameter range, the variation trends of motion amplitudes with wave period are broadly similar under both wave-only and wave-current conditions. However, the introduction of a uniform current has a non-negligible quantitative impact. It induces a significant, velocity-dependent mean drift force (manifested as offsets in the mean values) and substantially alters the motion amplitudes. This indicates that the incident waves serve as the primary energy source exciting the periodic oscillation of the FPSO, determining the fundamental frequency characteristics and overall trend of the response. In contrast, the superimposed steady current systematically modifies the equilibrium position via a constant drag force and quantitatively modulates the oscillation amplitudes by altering the surrounding flow field and vortex dynamics.

In terms of surge motion, as the wave period increases, the variation of motion amplitude with wave period is not very pronounced in both conditions. Under most wave periods, the surge amplitude in the wave-current condition is higher than that in the pure wave condition. As shown in Fig. 9, at wave periods of 10 s and 16 s, the amplitudes increase by 15.3% and 11.9%, respectively. However, the actual surge responses under these two periods are relatively small in magnitude. In contrast, at a wave period of 14 s, where the surge response is more significant, the amplitude increases by only 2%. These results indicate that the current has a noticeable amplifying effect on the wave-induced surge motion, and this amplification exhibits nonlinear characteristics with varying wave periods. Regarding the mean surge motion, due to the steady current force, the equilibrium position of the surge motion shifts significantly forward by 3.9 m to 4.5 m in the wave-current condition. The magnitude of this offset remains consistent across different wave periods, highlighting the considerable influence of current on the mean position of the structure.

For the heave motion, the difference in amplitude between the two conditions is generally within 5%, except at wave periods of 12 s and 14 s. At these periods, the heave amplitude increases by approximately 42.8% and 17.5%, respectively, under the wave-current condition. This suggests that the effect of current on heave motion is selective and more pronounced only at specific wave periods. Regarding the mean heave position, a downward offset of 0.03 m to 0.08 m in the heave equilibrium position occurred. This is attributed to flow separation induced by the presence of the current, which alters the flow structure beneath the platform and generates an additional downward force on the structure.

For the pitch motion, the amplitude under the wave-current condition is higher than that under the wave-only condition across all periods. The amplification is most significant near the natural period of pitch (around 16 s), which may indicate dynamic amplification due to fluid-structure interaction, where the amplitude increases by 99.4%. Additionally, the mean pitch angle shows a negative offset between 0.5° and 1.0° under the wave-current condition. This is caused by the yaw moment induced by the current, demonstrating that the current also has a steady influence on the attitude of the structure.

Analysis of the environmental loads acting on a FPSO unit is crucial as these loads directly determine the structural strength requirements and the design safety of the mooring system. Fig. 10 presents a comparative analysis of the mean values and amplitudes of the wave forces and mooring forces on a cylindrical FPSO under wave-only and wave-current coupling conditions across different wave periods.

In terms of wave force, the absolute value of the mean horizontal wave force under the combined wave-current condition is significantly larger than that under the pure wave condition. This is primarily because the measured total horizontal force includes a steady load component induced by the current. This component shifts the mean wave force in the negative direction by approximately 15,000 kN, resulting in an increase in the absolute value of the mean horizontal wave force. Regarding the amplitude of the wave force, the influence of the current shows clear period dependence. When the wave period is less than 14 s, the wave force amplitude is generally amplified. In contrast, when the wave period exceeds 14 s, the amplitude is suppressed. These observations indicate that the current not only introduces a steady load component but also nonlinearly modulates the amplitude characteristics of the dynamic wave load, reflecting the complex mechanism of wave-current interaction.

Regarding the mooring force, the steady-state force generated by the current acting on the hull is ultimately balanced by the mooring system. As a result, the mean mooring force under the combined wave-current condition increases significantly. This increase is primarily due to the larger mean surge motion induced by the current, reflecting the persistent influence of the current load on the static equilibrium of the system. In terms of the amplitude of the mooring force, the current suppresses its fluctuation, indicating that the current becomes the dominant factor affecting the dynamic variation of the mooring force. Under the influence of current, the distribution of wave energy is altered. As shown in Fig. 11, this significantly reduces the overall energy of mooring forces in the low-frequency band (e.g., at $\omega_1 = 0.0077$ Hz). Consequently, the large-amplitude slow-drift motion of the floating body is suppressed, leading to a more stable dynamic response of the mooring system.

4.2. Mechanism analysis of wave period influence

To investigate the wave-current coupling effects on the motion and load response of a cylindrical FPSO, this study compares the flow field structures under different wave periods. The aim is to reveal the underlying flow characteristics and physical mechanisms. The observed mechanistic differences can be explained by the key dimensionless parameter, the velocity ratio Uc/C (Sumer, 2006). The wave celerity C is positively correlated with the wave period T ($C \propto T$). Thus, for a constant current velocity Uc, a shorter wave period leads to a larger Uc/C ratio, indicating a more significant influence of the current.

A significant motion amplification was observed under the wave period of 16s, which is close to the structure's natural period. However, the load amplification induced by wave-current coupling is relatively limited. In this case, the higher wave celerity C results in a lower Uc/C ratio ($Uc/C < 0.25$), indicating that the flow field is dominated by wave-induced oscillations. Flow field analysis in Fig. 12 also shows that under

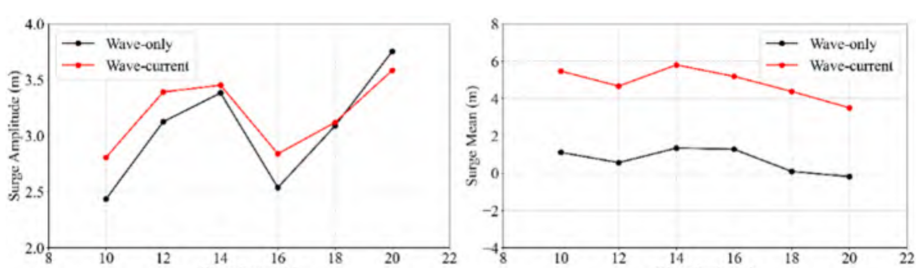

Fig. 6. Statistical characteristics of surge motion under different wave periods (a) amplitude value; (b) mean value (Results for wave-only condition, Uc = 0 m/s; results for wave-current condition, Uc = 0.2 m/s).

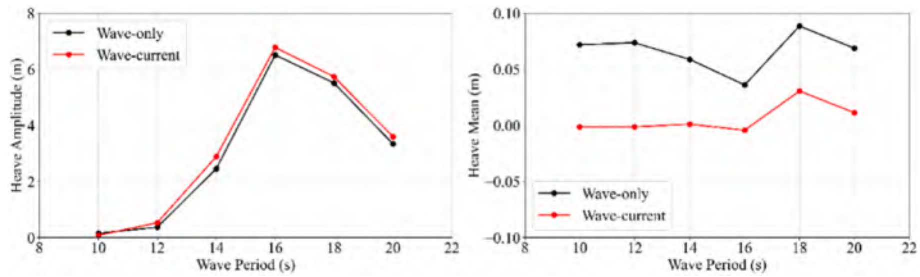

Fig. 7. Statistical characteristics of heave motion under different wave periods (a) amplitude value; (b) mean value (Results for wave-only condition, Uc = 0 m/s; results for wave-current condition, Uc = 0.2 m/s).

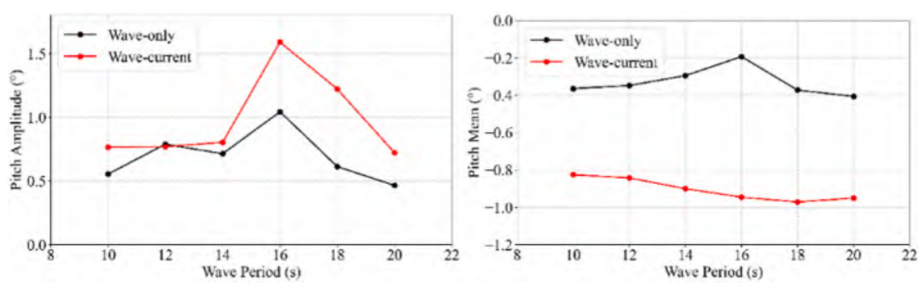

Fig. 8. Statistical characteristics of pitch motion under different wave periods (a) amplitude value; (b) mean value (Results for wave-only condition, Uc = 0 m/s; results for wave-current condition, Uc = 0.2 m/s).

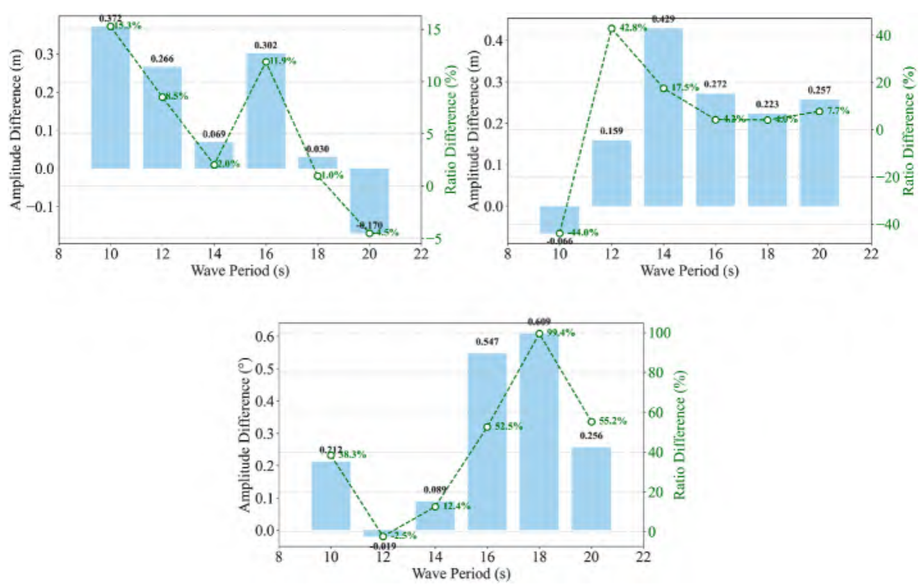

Fig. 9. Amplitude difference of motion under different wave periods (a) Surge; (b) Heave; (c)Pitch.

pure wave action, resonance has already generated a strong oscillatory flow with high velocities around the structure. After introducing the current, wave-current coupling induces noticeable low-velocity regions near the bottom and wake of the structure. Nevertheless, the overall flow pattern remains governed by wave motion. The underlying mechanism is that under resonance conditions, the energy input from waves is dominant. The nonlinear superposition effect contributed by the current as an additional energy source is relatively weak. As a result, the flow field's energy scale and structure are not fundamentally altered, leading to limited load amplification.

Conversely, under the wave period of 14s, which is a non-resonant period, wave-current coupling induces a more prominent amplification of heave motion and load. The flow characteristics for this case are distinctly different from those of the 16s period. Under wave action alone, the flow kinetic energy is relatively weak due to the deviation from the structural natural period. The introduction of the current markedly alters the flow structure, generating large transient high-velocity zones beneath and around the structure, with velocities substantially higher than in the wave-only case, as demonstrated in Fig. 13. The underlying mechanism lies in the decreased wave celerity C at the shorter wave period. Although the Uc/C ratio remains small and waves still dominate the overall flow, the increase in Uc/C enhances the contribution of the current to the nonlinear coupling process. This strengthened nonlinear superposition effect significantly raises flow kinetic energy and asymmetry. As a result, although the absolute heave response under waves alone is smaller than in the 16-s resonant case, the

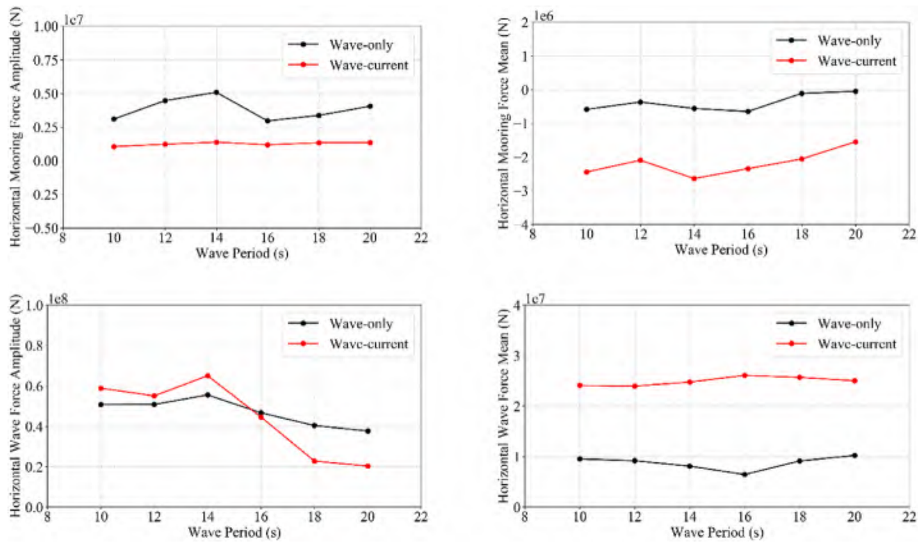

Fig. 10. Statistical characteristics of load under different wave periods (a) horizontal mooring force; (b) horizontal wave force (Results for wave-only condition, Uc = 0 m/s; results for wave-current condition, Uc = 0.2 m/s).

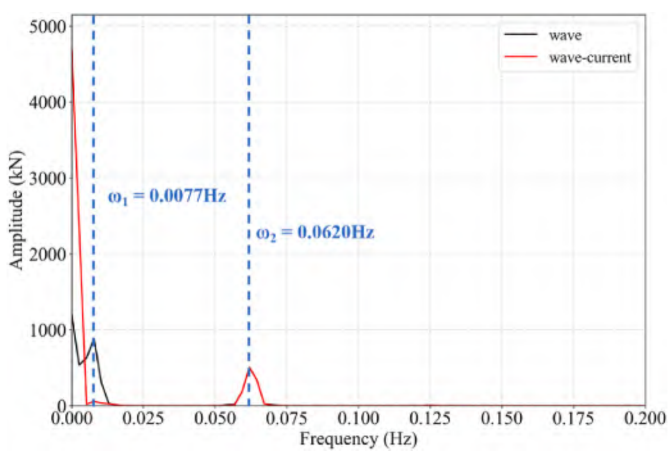

Fig. 11. Spectral analysis of the horizontal mooring force (wave periods = 16s).

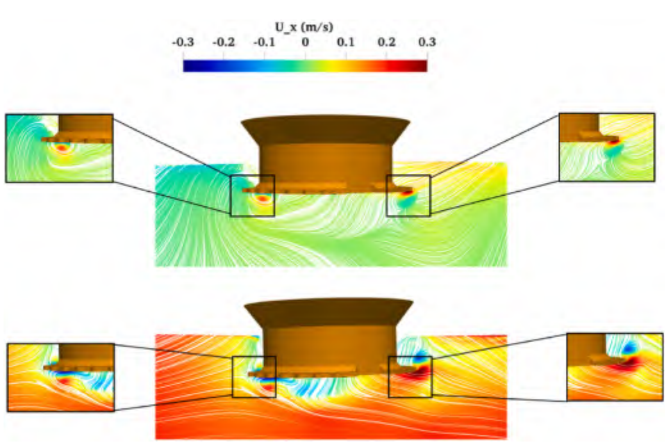

Fig. 12. Comparison of Velocity Fields under Wave Condition and Coupled Wave-Current Condition (Wave periods = 16s).

relative amplification of heave motion in the 14-s case is greater. This leads to more severe instantaneous wave loads in the time domain compared to the resonant condition.

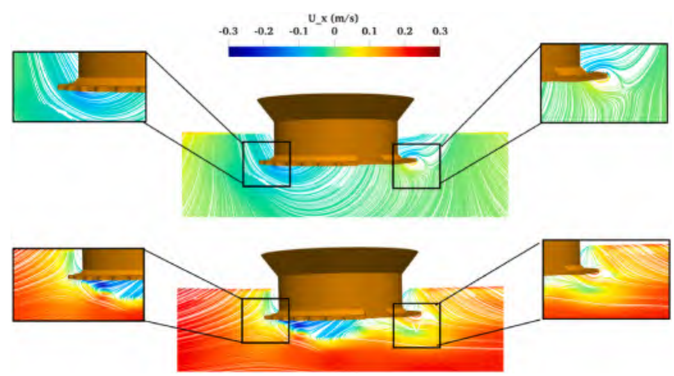

Fig. 13. Comparison of Velocity Fields under Wave Condition and Coupled Wave-Current Condition (Wave periods = 14s).

The non-monotonic trend of heave amplification, with a peak at T = 12s, suggests that the Uc/C ratio alone is not sufficient to predict the response. The maximum amplification likely occurs at an optimum coupling condition, where the wave period allows the current-modified vortex shedding from the heave plates to achieve a phase-lock that most constructively excites the heave mode.

Furthermore, wave-current coupling causes constant mean position offsets of the structure, including a forward shift in surge, sinking in heave, and a negative pitch angle. This steady-state phenomenon originates from the disruption of flow field symmetry around the structure. Flow contour plots clearly show that the current causes a persistent low-velocity zone in the wake and a significant velocity reduction at the bottom of the cylinder FPSO. As illustrated in Figs. 14 and 15, the physical mechanism is as follows: the wake low-velocity zone creates a pressure difference, generating a viscous pressure resistance in the direction of the current; the low-velocity zone at the bottom leads to a pressure reduction, causing a downward suction force; meanwhile, the point of action of the current force is below the center of rotation, creating an overturning moment. The combined forces and moments generated by this steady-state component of the flow field directly lead to the shift in the structure's equilibrium position.

This study further conducted a comparative analysis of the mid-longitudinal vorticity fields under wave-only and wave-current coupled conditions. Taking the 16-s wave period case as an example,

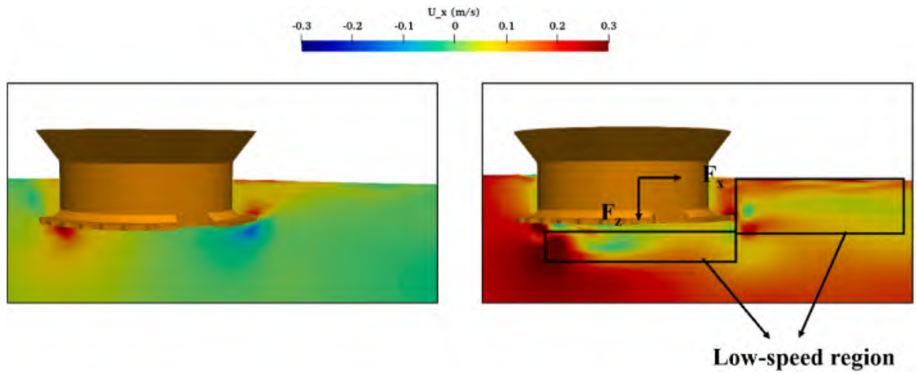

Fig. 14. Comparison of Velocity Fields Wave Condition and Coupled Wave-Current Condition (Wave periods = 16s).

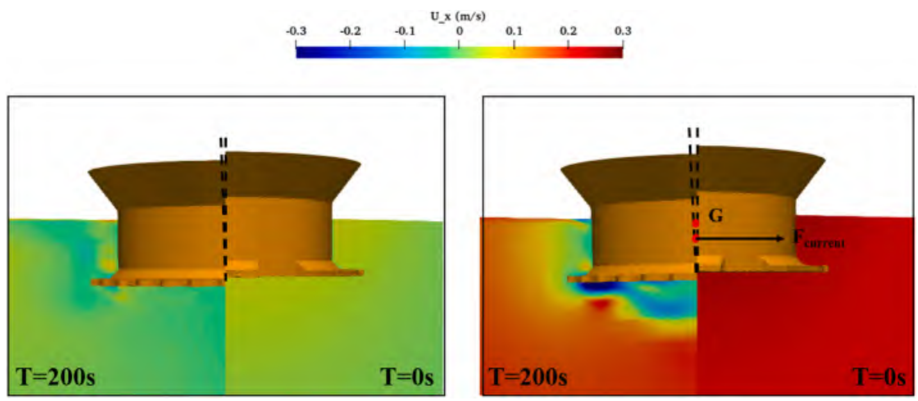

Fig. 15. Comparison of Velocity Fields Wave Condition and Coupled Wave-Current Condition (Wave periods = 16s).

Fig. 16 reveals significant structural differences between the vorticity fields under wave-only and wave-current coupled conditions. Under wave-only conditions, the vorticity generated by structural motion is primarily concentrated near the cylinder bottom and the heave plate. In contrast, under wave-current coupled conditions, the presence of background flow leads to a clear accumulation of negative vorticity at the cylinder bottom. Simultaneously, the current continuously transports vorticity downstream, resulting in a much wider distribution of vorticity in the wake region compared to the wave-only case. This significantly enhances the complexity of the flow field and the intensity of vortex motion, thereby amplifying the heave and surge motions of the structure.

4.3. Wave-current coupling effects across different current velocity

Fig. 17 compares the surge, heave, and pitch motion responses of a cylindrical FPSO under a 14-s wave period and different current velocities, focusing on variations in the mean and amplitude of each motion. As the current velocity increases, the mean surge increases significantly from 1.01 m to 5.80 m, a rise of over four times, indicating notable horizontal drift of the FPSO due to steady drag force induced by the current. The surge amplitude also shows an increasing trend, further demonstrating that wave-current coupling amplifies the horizontal motion. For pitch motion, the mean value changes from -0.30° to -0.92°, suggesting that the current exerts a continuous bow-down moment on the hull, likely due to asymmetric pressure distribution around the structure. The pitch amplitude increases from 1.17° to 2.56°, a rise of about twofold, indicating that the current significantly enhances

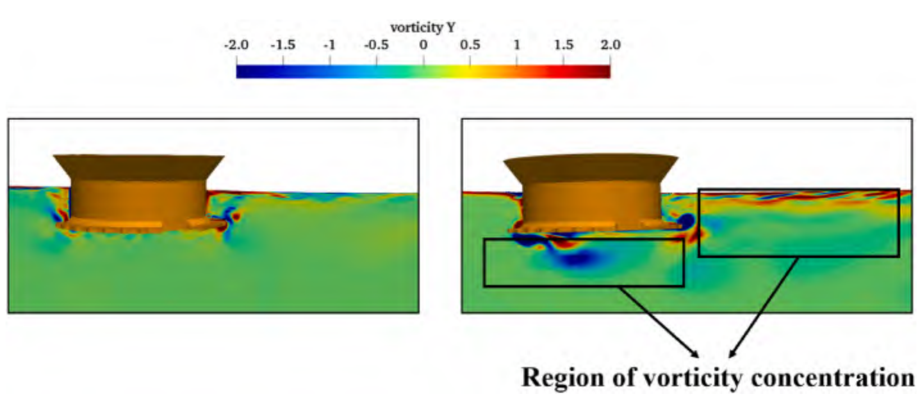

Fig. 16. Comparison of Vorticity Contour between Wave Condition and Coupled Wave-Current Condition (Wave periods = 16s).

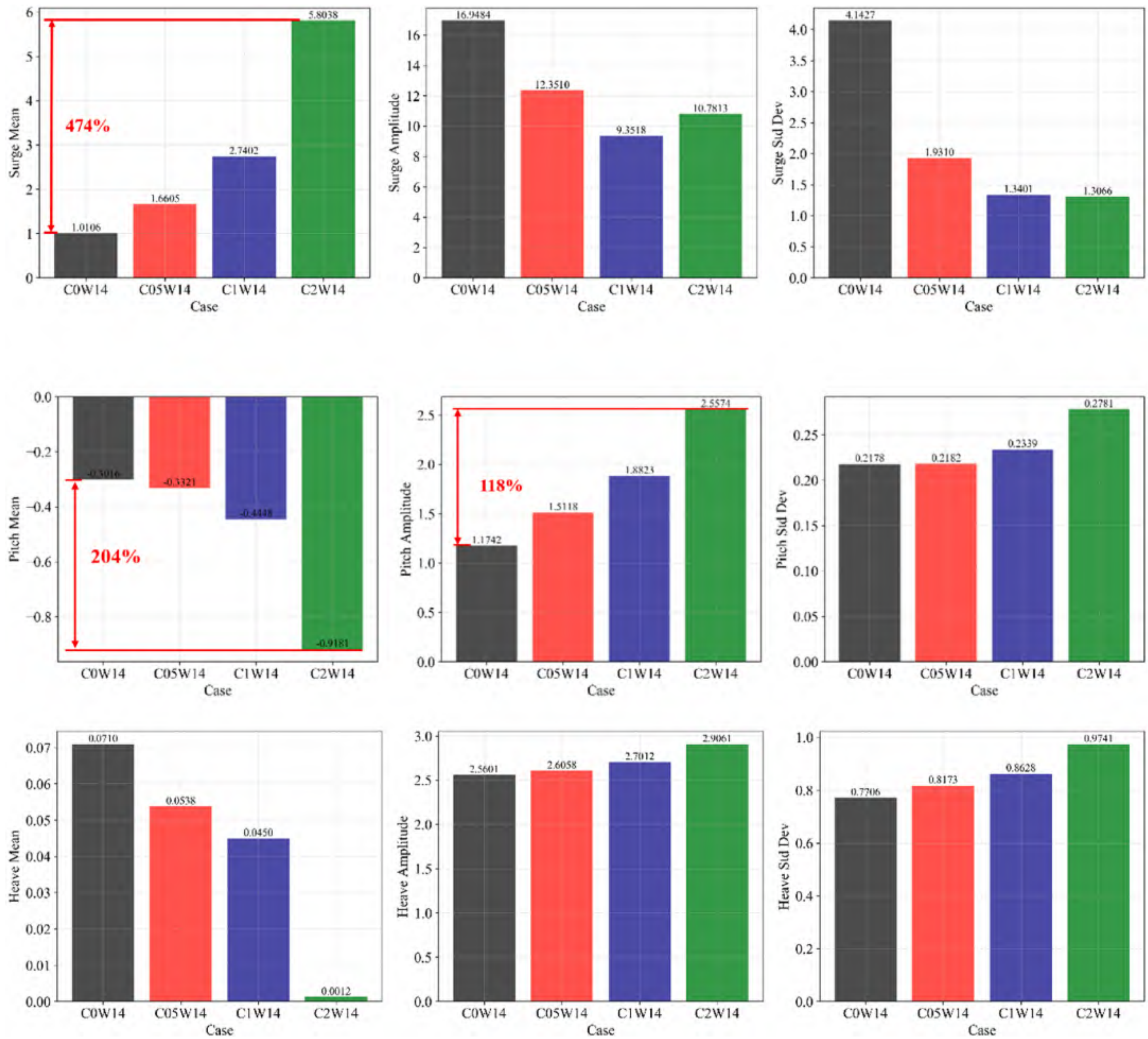

Fig. 17. Statistical characteristics of motion under different current velocities (a) surge motion; (b) heave motion; (c) pitch motion.

the rotational response, with more pronounced dynamic amplification at higher current velocities. The mean heave slightly decreases from 0.071 m to 0.001 m, implying limited influence of the current on the vertical stationary position. However, the heave amplitude increases from 2.61 m to 2.91 m, and the standard deviation rises from 0.77 to 0.97. This shows that although the mean position remains stable, both the magnitude and randomness of the dynamic motion increase with current velocity, resulting in a more complex motion response.

In summary, increased current velocity systematically influences the FPSO's motion. Horizontal motion is dominated by current-induced static offset, while rotational and vertical motions exhibit amplified dynamic components and enhanced randomness.

Fig. 18 compares the mean values and amplitudes of the wave forces and mooring forces on a cylindrical FPSO under pure wave and wave-current coupled conditions, using a 14-s wave period and different current velocities. For the horizontal wave force, the mean value increases sharply from 7665.77 kN under the no-current condition to 24,940.29 kN under the high-current condition, an increase of more than two times. This indicates that the wave force includes a significant steady-state component induced by the current. A higher current velocity leads to a greater sustained horizontal thrust on the hull. The amplitude also rises from 56,232.12 kN to 67,199.77 kN, showing that the current not only introduces a static load but also nonlinearly amplifies the dynamic wave load by altering the relative motion between the waves and the structure.

The horizontal mooring force shows a similar trend to the horizontal wave force. To balance the large horizontal thrust acting on the structure, the mooring system must provide a greater reaction force. As a result, the mean mooring force also increases significantly with current velocity. In contrast, the fluctuating component of the mooring force decreases as the current velocity increases. This finding supports the previous analysis: the current alters the energy distribution of the wave forces, thereby significantly suppressing the low-frequency components in the mooring force. As the current velocity strengthens, this suppressive effect becomes more pronounced. The dynamic response of the mooring system becomes more stable, and the overall system behavior

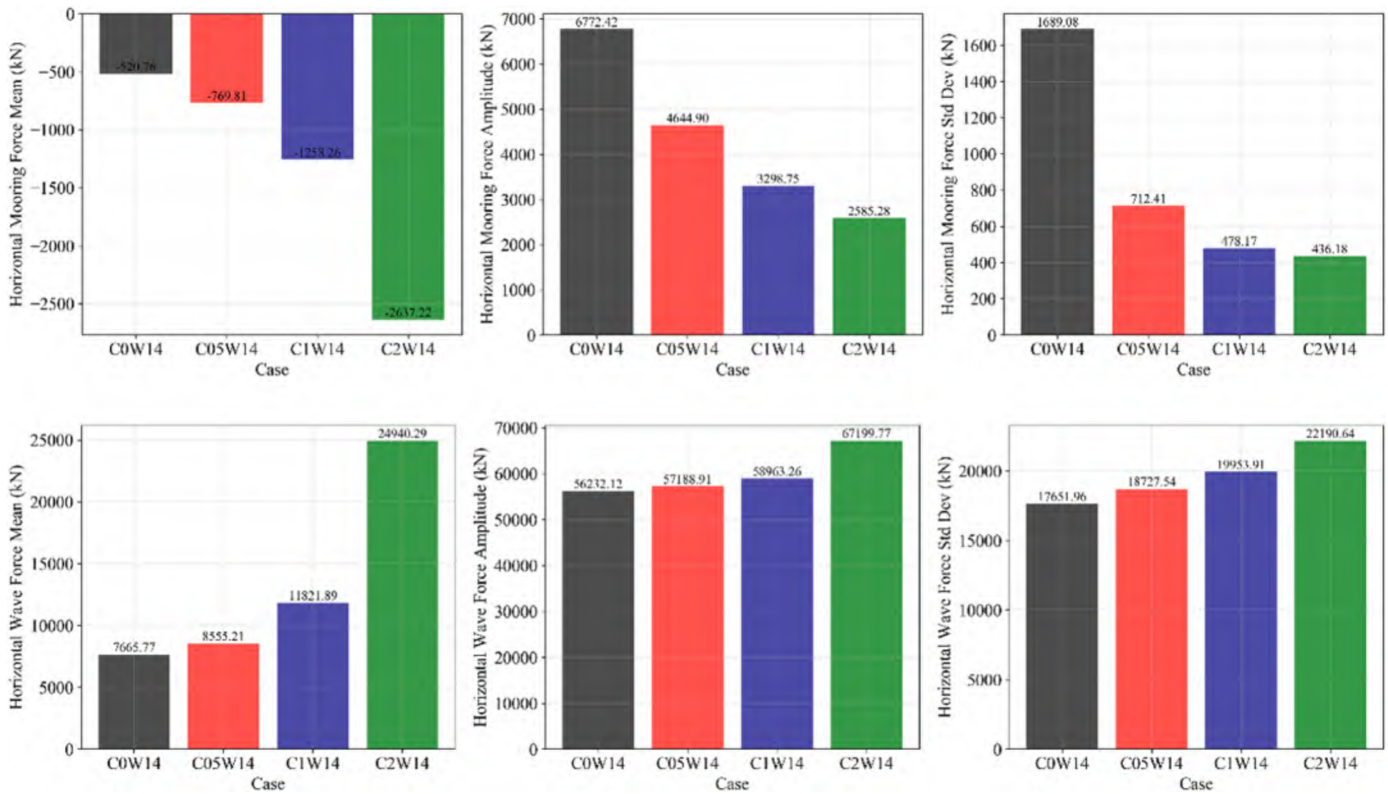

Fig. 18. Statistical characteristics of load under different current velocities (a) horizontal mooring force; (b) horizontal wave force.

transitions toward being predominantly governed by the current load.

The preceding analysis focuses on the amplitude of the motions and loads, defined as the peak-to-peak value during steady-state response. To provide a more robust quantification of the dynamic fluctuation intensity and to assess the change in signal randomness with current velocity, we have further computed the standard deviation of the key responses. As shown in Fig. 17, the standard deviation of the heave motion increases markedly with the current velocity, rising from 0.77 m to 0.97 m. This trend is consistent with the observed increase in heave amplitude. More importantly, the standard deviation more clearly reveals that increasing the current velocity not only enlarges the typical oscillatory range but also systematically intensifies the random fluctuation component of the motion. Similarly, the standard deviation of the pitch motion exhibits a definitive increasing trend. These findings support the conclusion that a uniform current exacerbates the unsteadiness and asymmetry of the flow field, thereby enhancing the stochastic dynamic characteristics of the motion responses.

4.4. Mechanism investigation of the current velocity effect

To deeply investigate the mechanism behind the amplification effects of current velocity on the motion and loads of a cylindrical FPSO, this study compares and analyzes the flow field structures under different current velocities. The aim is to reveal the underlying flow characteristics and physical mechanisms. To support quantitative analysis, five measurement points are set up, as shown in Fig. 19. The mean pressure and pressure amplitude at these points are compared across four working conditions, in order to validate the variation patterns of the flow field properties.

Fig. 20 illustrates the instantaneous flow fields at a certain moment under different current velocities. Under zero flow velocity, the velocity field is uniform, and the fluid is nearly stationary, with no macroscopic flow observed. As a result, there is no significant kinetic energy or velocity gradient. At low flow velocity, a distinct velocity distribution

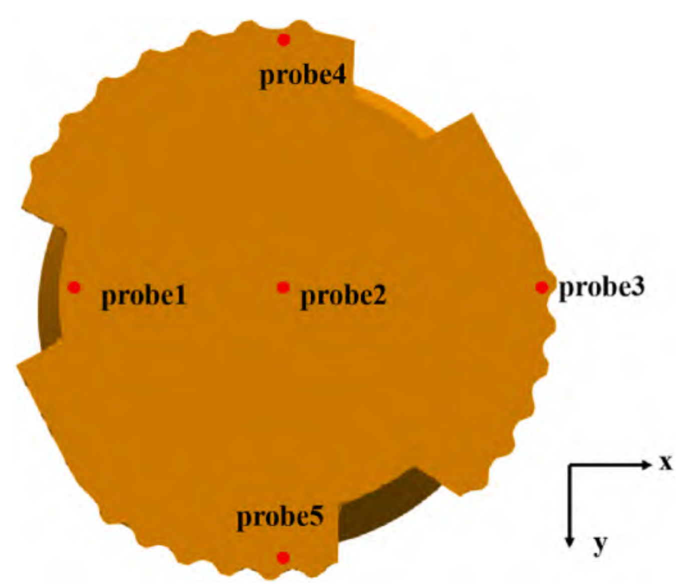

Fig. 19. Locations of the pressure probes.

begins to appear. The fluid accelerates as it passes around the structure, forming a low-speed wake region behind the structure that is not yet fully developed. At this stage, a velocity gradient exists but remains relatively weak. As the incoming flow velocity increases, the acceleration effect around the structure becomes more pronounced, leading to a stronger velocity contrast in the wake region.

The amplification of surge motion is primarily dominated by pressure drag. Fig. 18 presents a comparison of the differential pressure drag under four different flow velocities. At low flow velocity, the motion is driven by a stable pressure difference between the high-speed region in

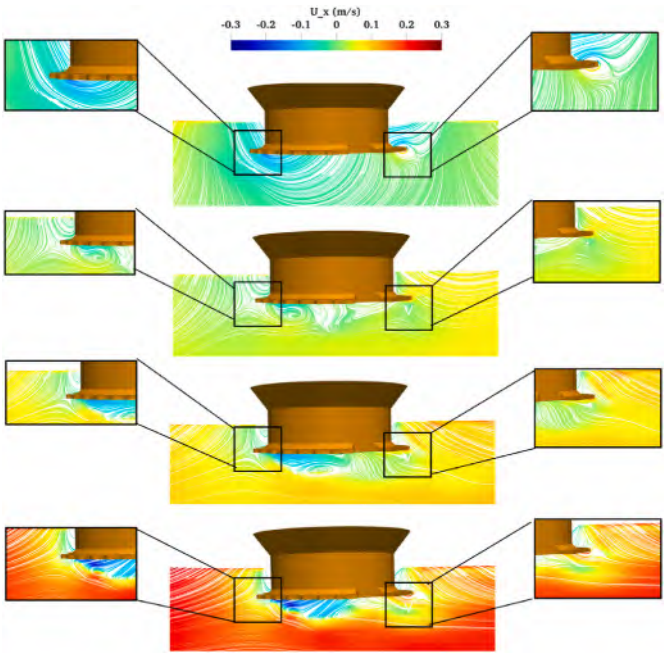

Fig. 20. Comparison of velocity fields under different current velocities (a) C0W14; (b) C05W14; (c) C1W14; (d) C2W14.

front of the structure and the low-speed wake region behind it. In this case, the amplification effect remains relatively linear. Under high flow velocity, however, the amplification increases nonlinearly. This is because both the extent and intensity of the low-pressure region in the wake increase significantly. As a result, the pressure drag no longer grows simply with the square of the flow velocity, but exhibits a stronger amplification, leading to a notable increase in the dynamic amplitude of the surge motion.

The amplification of the pitch motion originates from the asymmetry in the velocity distribution over the upper and lower surfaces of the structure. This asymmetry induces a pressure difference, which generates a moment. As shown in Fig. 21, pressure data from five measuring points at the bottom of the structure are provided. A comparison of the pressures at probe1 and probe3 indicates that this asymmetry is relatively weak under low flow velocity. At high flow velocity, however, flow separation at the bottom becomes more intense, while the flow over the top remains relatively smooth. This spatial asymmetry in the velocity field is significantly amplified, leading to a substantial increase in both the steady bow-down moment and its fluctuating component. As a result, both the static offset and dynamic amplitude of the pitch motion are markedly amplified.

The amplification of heave motion is primarily dominated by pressure fluctuations at the bottom of the structure. The mean heave displacement changes little, because the variation in flow velocity generates only a small average lift force. However, the amplification of its dynamic amplitude is distinct—it depends not on a steady velocity difference, but on instantaneous fluctuations in the velocity field. As also reflected by the comparison of pressure amplitudes at the bottom measurement points probe1 to probe5 in Fig. 22, the velocity field below the structure becomes highly complex and unsteady under high flow conditions. This translates directly into intense and random pressure fluctuations acting on the bottom surface. As the flow velocity increases, both the intensity and frequency of the velocity fluctuations beneath the structure rise, leading to a significant amplification in the randomness and amplitude of the heave motion. This mechanism is fundamentally different from those governing surge and pitch amplification.

This study further compares and analyzes the evolution of the vorticity field along the centerline plane under different current velocities. Fig. 23 shows the instantaneous vorticity fields at a certain moment

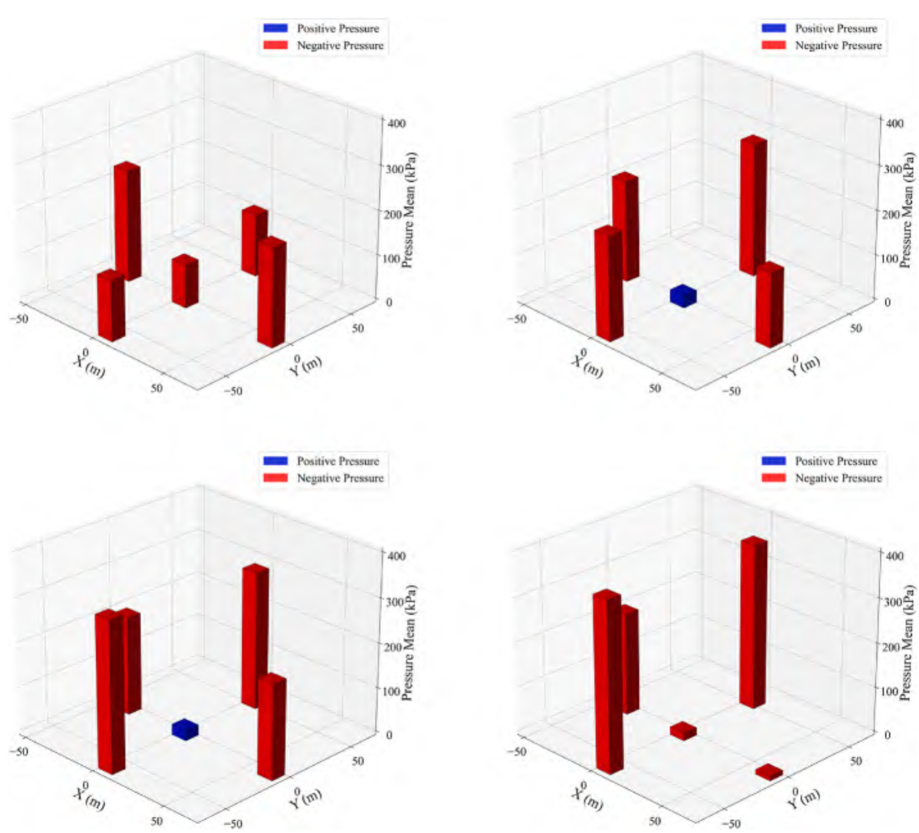

Fig. 21. Comparison of pressure mean for probes (a) C0W14; (b) C05W14; (c) C1W14; (d) C2W14.

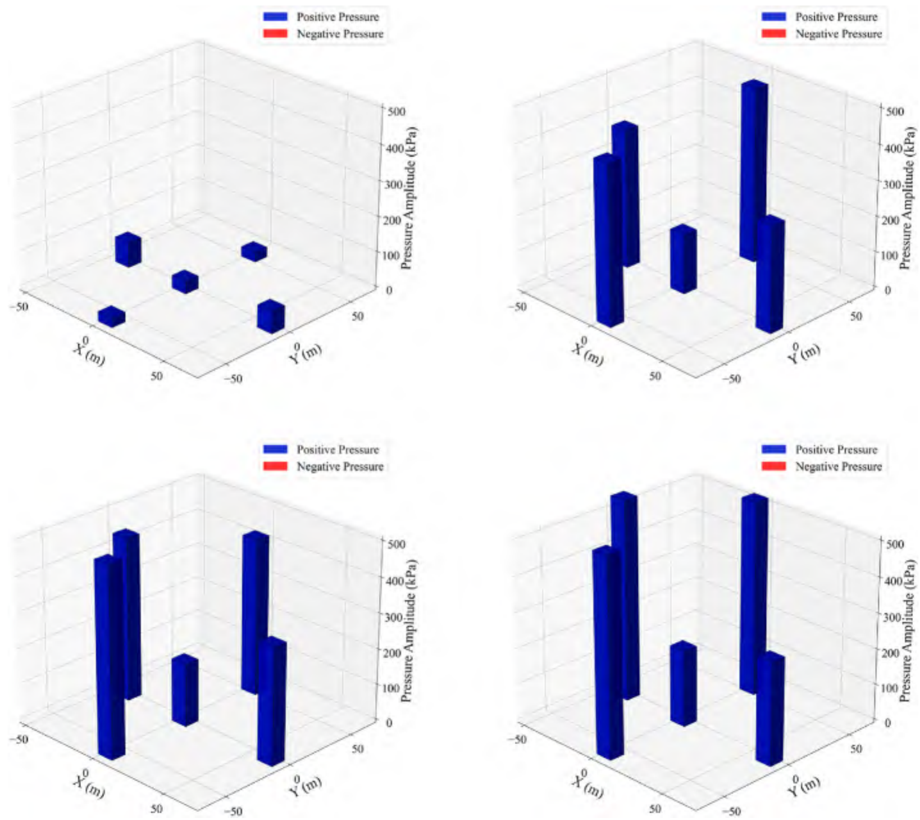

Fig. 22. Comparison of pressure amplitude for probes (a) C0W14; (b) C05W14; (c) C1W14; (d) C2W14.

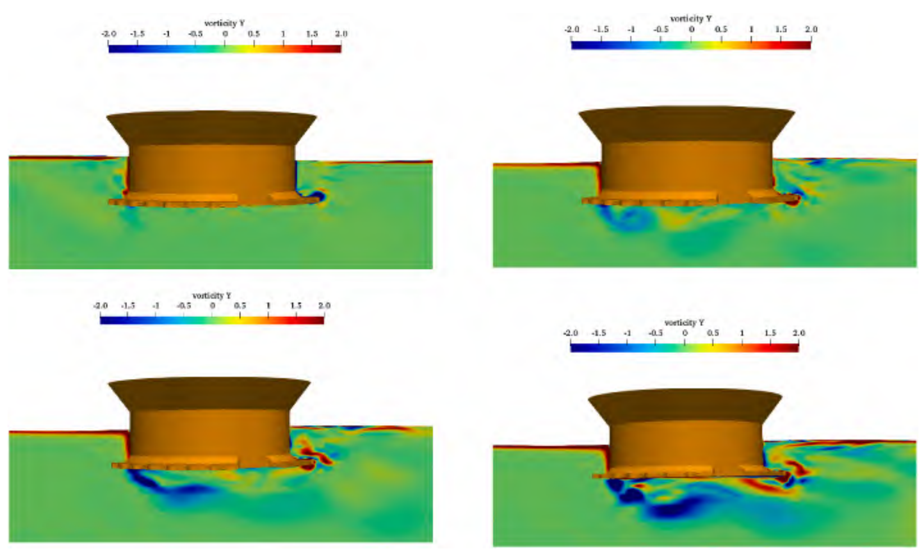

Fig. 23. Comparison of vorticity fields under different current velocities (a) C0W14; (b) C05W14; (c) C1W14; (d) C2W14.

under the four working conditions.

The amplification of surge motion shows distinct characteristics at different flow velocities. Under zero flow velocity, there is no significant flow separation, and surge is mainly induced by wave forces, with minimal mean offset. As flow velocity begins, small-scale vortices start to form at the stern, leading to the initial development of pressure drag. This results in an observable steady drift in surge. With a further increase in flow velocity, flow separation evolves from being localized to large-scale vortex shedding. This transition causes the pressure drag to increase nonlinearly rather than linearly, leading to a disproportionate amplification in the mean surge displacement.

The amplification of pitch motion strongly depends on the influence of flow velocity on the spatial structure of vortices. Fig. 24 provides direct evidence of this relationship, comparing the vortex evolution over a 14-s wave period with and without a 0.2 m/s current. The wave-only condition (Uc = 0 m/s) corresponds to a low-flow-velocity state, where the vortices near the bottom are weak and small in scale. These vortices generate only a limited bow-down moment, resulting in a minor pitch response. In contrast, the high-flow-velocity condition (Uc = 0.2 m/s) produces a significant increase in vortex intensity and scale, accompanied by more pronounced asymmetry. As a result, the steady mean pitch increases with flow velocity, while the dynamic response is amplified

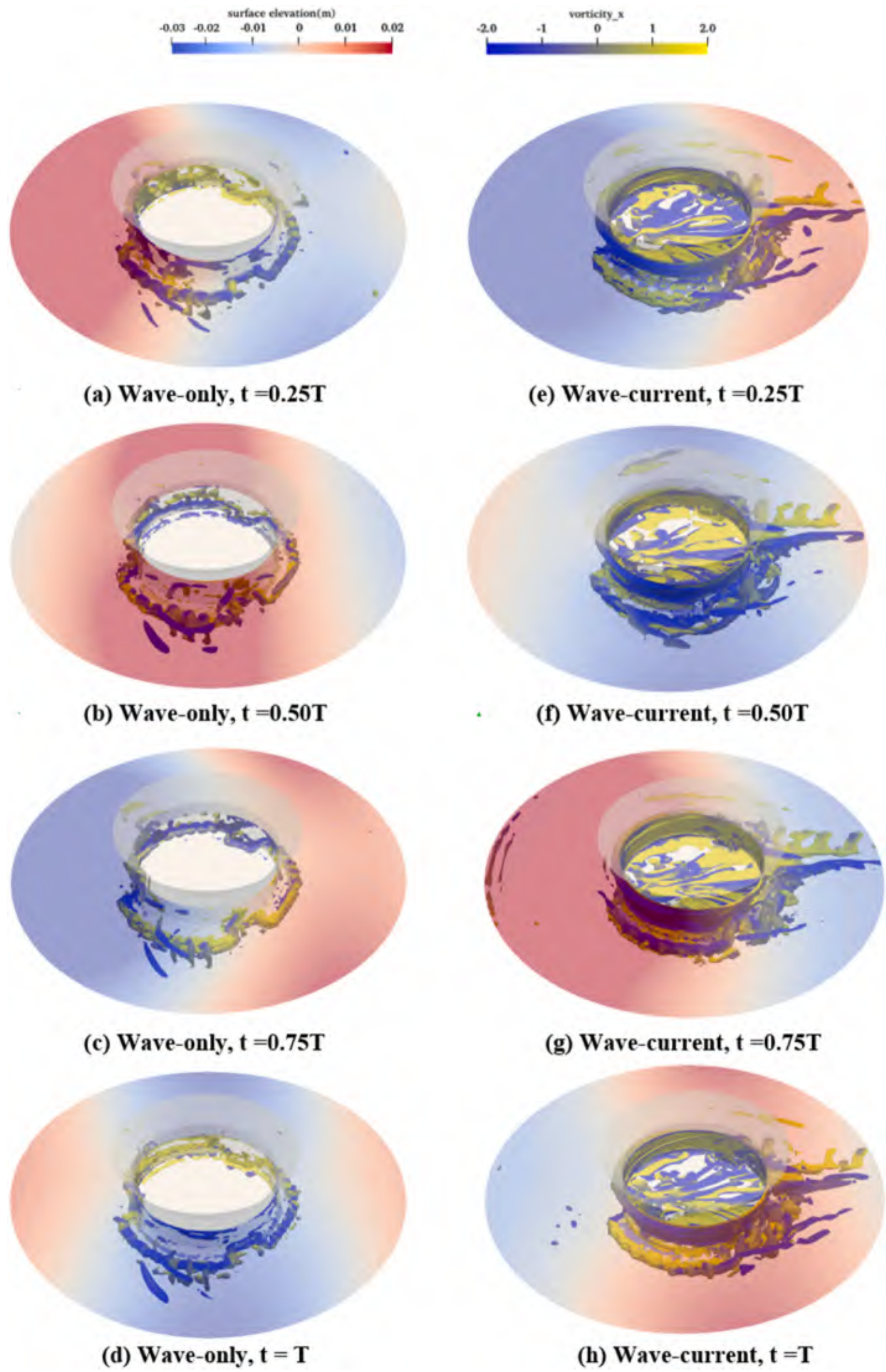

Fig. 24. 3D vortex structures over one wave period (T = 14 s) under wave-only (a–d, Uc = 0 m/s) and wave-current (e–h, Uc = 0.2 m/s) conditions.

even more noticeably. This is because the unsteady and asymmetric vortex shedding generates stronger wave-induced moments, whose excitation frequency and energy increase with flow velocity, leading to a multiplied amplification in pitch amplitude at higher flow velocities.

The dynamic amplification of heave motion exhibits unique sensitivity to flow velocity. Its mean value is governed by static equilibrium and is therefore hardly affected by flow velocity. However, the amplification of its dynamic response shows a highly nonlinear relationship with flow velocity. At low velocity, the weak bottom vortices cause little disturbance to the vertical pressure field, and heave motion is dominated primarily by wave frequency. Similarly, Fig. 24 demonstrates that moderate to high flow velocities trigger large-scale vortex shedding at the bottom, leading to intense local pressure pulses. Each strong vortex shedding acts like an instantaneous vertical impact. As the flow velocity increases, the intensity, frequency, and randomness of these impacts rise significantly. Consequently, beyond a certain velocity threshold, the complexity and randomness of the heave motion are markedly amplified, reflected in a substantial increase in standard deviation and amplitude.

5. Conclusion

This study employs the open-source CFD software OpenFOAM to systematically simulate the motion and load responses of a cylindrical

FPSO under various wave periods and current velocities. By comparing coupled wave-current conditions with wave-only conditions, the amplification effects are quantified. Furthermore, the patterns and underlying physical mechanisms of these effects are revealed from the perspective of flow field evolution. The main conclusions are as follows.

(1) The motion and load responses of the CFPSO are primarily excited by the incident waves, which determine the basic response frequency and trend. Under wave-current coupling, the superimposed current introduces significant quantitative modifications. Its influence is characterized by introducing significant steady-state components and nonlinearly modulating dynamic components. The steady drag force from the current causes notable changes in the structure's mean position, such as a forward offset in surge and a negative bias in pitch. It also directly increases the mean wave force and mooring load. Concurrently, through nonlinear interaction with waves, the current selectively amplifies (especially at non-resonant periods) or suppresses (e.g., fluctuations in mooring force) the dynamic amplitudes of motion and load. This effect varies nonlinearly with wave period and current velocity.

(2) The wave period determines the dominant mechanism of the wave-current coupling effect, and the current-to-wave velocity ratio (Uc/C) is a key dimensionless parameter. Under conditions close to the structure's natural period (e.g., T = 16 s), the motion response is dominated by wave energy, and the additional nonlinear amplification from the current is relatively weak. In contrast, at non-resonant periods (e.g., T = 14 s), the increased Uc/C value enhances the current's contribution to flow field kinetic energy and asymmetry. The nonlinear superposition effect becomes more prominent, potentially leading to more significant instantaneous heave motion amplification and load response than under resonant conditions.

(3) The amplification mechanisms differ fundamentally for various motion directions, rooted in changes in the flow field structure. Surge amplification is primarily driven by a steady pressure difference resistance caused by the current. Pitch amplification originates from an asymmetric velocity distribution, which creates steady and dynamic moments. In contrast, the dynamic amplification of heave is directly related to intense, random pressure fluctuations induced by complex vortex shedding near the bottom. As the current velocity increases, the development in intensity, scale, and asymmetry of the wake vortex system is the fundamental physical reason for the nonlinear amplification of surge and pitch responses and the increased randomness of heave motion.

The ultimate motion and load response are not determined by the Uc/C ratio alone, but rather by its interplay with the structure's inherent hydrodynamic properties. To develop more comprehensive design guidelines, future research is needed to systematically explore a wider Uc/C parameter space. Such work would fully map the response sensitivities and identify potential thresholds for transitions between different flow-dominance regimes.

CRediT authorship contribution statement

Min Li: Writing – original draft, Methodology, Data curation. **Da Li:** Investigation, Formal analysis, Conceptualization. **Shenglei Fu:** Visualization, Investigation, Conceptualization. **Yuan Zhuang:** Writing – review & editing, Validation, Methodology. **Decheng Wan:** Supervision, Resources, Methodology.

Author declarations

Authors have no conflict of interest to declare.

Declaration of competing interest

The authors declare that they have no known competing financial interests or personal relationships that could have appeared to influence the work reported in this paper.

Acknowledgements

This work is supported by the National Key Research and Development Program of China (Grant No. 2025YFF0519800), and National Natural Science Foundation of China (No. 52131102), to which the authors are most grateful.

Data availability

The data that support the findings of this study are available from the corresponding author upon reasonable request.

References

Amin, I., Dai, S., Day, S., et al., 2022. Experimental investigation on the influence of interceptor plate on the motion performance of a cylindrical FPSO. Ocean. Eng. 243, 110339.
Afriana, R., 2011. Coupled Dynamic Analysis of Cylindrical FPSO, Moorings, and Riser Based on Numerical Simulation. University of Stavanger. Master's thesis.
Cui, Y., Li, Y., Li, G., et al., 2025. Dynamic response and nonlinear resonance of cylindrical FPSO with a ring groove considering time-varying restoring stiffness. Ocean. Eng. 325, 120857.
Deng, S., Cai, Y., Yang, X., et al., 2022a. Experimental study on the effects of wave and Current interaction on vertical motions of a cylindrical FPSO. In: ISOPE International Ocean and Polar Engineering Conference. ISOPE. ISOPE-I-22-172.
Deng, S., Zhong, W., Yang, X., et al., 2022b. Experimental and numerical study of the hydrodynamic features of a cylindrical FPSO considering current-induced motion. Ocean. Eng. 262, 112263.
Dutta, D., Afzal, M.S., 2024. Numerical investigation of hydrodynamic characteristics for flow past a square cylinder due to combined wave-current effect. Phys. Fluids 36 (7).
Higuera, P., Lara, J.L., Losada, I.J., 2013. Realistic wave generation and active wave absorption for navier–stokes models: application to OpenFOAM®. Coast. Eng. 71, 102–118.
Hirt, C.W., Nichols, B.D., 1981. Volume of fluid (VOF) method for the dynamics of free boundaries. J. Comput. Phys. 39 (1), 201–225.
Hong, S.K., Yuck, R.H., Jang, B.S., et al., 2011. The investigation of non-linear effect for a circular cylinder shaped FPSO[C]. Int. Conf. Offshore Mech. Arctic Eng. 44359, 837–845.
Huo, S., Deng, S., Song, Z., et al., 2023. On the hydrodynamic response and slamming impact of a cylindrical FPSO in combined wave-current flows. Ocean. Eng. 275, 114139.
Ji, X., Li, Y., Tang, Y., et al., 2019. Damping performance of annular anti-motion structures on a cylindrical floating drilling production storage and offloading system. Ocean. Eng. 192, 106590.
Jacobsen, N.G., Fuhrman, D.R., Fredsøe, J., 2012. A wave generation toolbox for the open-source CFD library: openfoam®. Int. J. Numer. Methods Fluid. 70 (9), 1073–1088.
Kim, W.B., Sung, G.H., Kim, H.J., et al., 2013. Comparison of linear spring and nonlinear FEM methods in dynamic coupled analysis of floating structure and mooring system. J. Fluid Struct. 42, 205–227.
Kong, M., Zhang, X., Ji, R., et al., 2025. Effects of wave–current interaction on hydrodynamic performance and motion response of a floating tidal stream turbine. J. Mar. Sci. Eng. 13 (8), 1520.
Li, D., Duan, W., Huang, L., et al., 2024. Effects of the current-wave interaction on a cylinder platform. Ships Offshore Struct. 19 (7), 935–947.
Li, S., Hao, J., Ren, Y., et al., 2025. Numerical modeling of a triangle semi-submersible floating wind platform under wave–current flows. J. Mar. Sci. Eng. 13 (4), 714.
Li, W., Ke, S., Qian, K., et al., 2025. Instability mechanism and criterion of wind-wave co-generation structural system under typhoon-wave-current coupled action. Renew. Energy, 123888.
Li, X., Xiao, Q., Wang, E., et al., 2023. The dynamic response of floating offshore wind turbine platform in wave–current condition. Phys. Fluids 35 (8).
Liu, Y., Wan, D., 2013. Numerical simulation of motion response of an offshore observation platform in waves. J. Mar. Sci. Appl. 12 (1), 89–97.
Menter, F.R., Kuntz, M., Langtry, R., 2003. Ten years of industrial experience with the SST turbulence model. Turbulence, heat and mass transfer 4 (1), 625–632.
Menter, F.R., 1994. Two-equation eddy-viscosity turbulence models for engineering applications. AIAA J. 32 (8), 1598–1605.
Ni, M., Wei, K., Wang, J., et al., 2025. Steady-state solution for wave−current interactions between third-order wave and oblique current based on numerical basin simulation. Ocean. Eng. 341, 122780.
Sumer, B.M., 2006. Hydrodynamics Around Cylindrical Strucures[M]. World scientific.
Van Maele, K., Merci, B., 2006. Application of two buoyancy-modified k–ε turbulence models to different types of buoyant plumes. Fire Saf. J. 41 (2), 122–138.

Wang, J., Wan, D., 2018. CFD investigations of ship maneuvering in waves using naoe-FOAM-SJTU solver. J. Mar. Sci. Appl. 17 (3), 443–458.
Wang, J., Zhao, W., Wan, D., 2019. Development of naoe-FOAM-SJTU solver based on OpenFOAM for marine hydrodynamics. J. Hydrodyn. 31 (1), 1–20.
Wang, P., Yu, W., Zhao, M., et al., 2024. Effects of wind-wave-current-earthquake interaction on the wave height and hydrodynamic pressure based on CFD method. Ocean. Eng. 305, 117909.
Wang, W., Piao, T., Geng, C., et al., 2024. Slamming characteristics due to the special shape of new sandglass-type model in waves by comparing with cylindrical model. J. Mar. Sci. Eng. 12 (5), 712.
Yang, C., Lu, Z., Wan, C., et al., 2025. Semi-analytical study on the hydrodynamic performance of a cylindrical moon column FPSO with damping plate. Ocean. Eng. 316, 119894.
Yu, W., Wang, P., Zhao, M., et al., 2025. Fluid-structure interaction simulation of floating structure interacting with the combined effect of wave-current-earthquake based on CFD method. Ocean. Eng. 339, 122192.
Zhao, W., Wang, J., Wan, D., 2020. Vortex identification methods in marine hydrodynamics. J. Hydrodyn. 32 (2), 286–295.
Zhou, X., Jiang, Q., Wang, Y., et al., 2022. Numerical simulation of wave–current force characteristics of horizontal floating cylinder in heave motion. J. Mar. Sci. Eng. 10 (12), 1884.
Zhuang, Y., Wang, G., Wan, D., et al., 2022. Numerical simulations of FPSO with sloshing tanks in a random freak waves. J. Hydrodyn. 34 (3), 491–498.